Search for New Particles Decaying to Hadronic Jets in Proton-Proton Collision at $\sqrt{s} = 13$ TeV

by

Karishma Sekhon

A dissertation submitted in partial fulfillment
of the requirements for the degree of
Doctor of Philosophy
(Physics)
in The University of Michigan
2018

Doctoral Committee:

Professor Dante Amidei, Chair
Associate Professor David Baker
Assistant Professor Emanuel Gull
Professor Aaron Pierce
Professor Jianming Qian

Karishma Sekhon

ksekhon@umich.edu

ORCID iD: 0000-0001-7677-8394

Dedicated to my beloved parents.

Acknowledgments

I would first and foremost like to thank my parents. Thank you so much for giving me the opportunity to follow my dreams! I would not be where I am today without your endless love, support and guidance. A big thanks to my grandparents and siblings for their constant love and support!

I would gratefully like to thank my advisor Dante Amidei. Dan, thank you for your immense patience, your teaching, your wisdom, your guidance, your protection and your freedom! SWIFT and this thesis would not have been possible without you. I will always be indebted to you for introducing me to Ryan!

At last I would like to thank my thesis committee members, my Michigan ATLAS mentors and friends, the High Mass Dijet team and all my ATLAS collaborators for the constant support, learning and fun times! I had a blast knowing and learning from you all. Thank you!

TABLE OF CONTENTS

LIST OF FIGURES

LIST OF TABLES

LIST OF APPENDICES

LIST OF ABBREVIATIONS

ATLAS A Toroidal LHC ApparatuS

BSM Beyond the Standard Model

CERN Center of European Nuclear Research

CSC Cathode Strip Chambers

CL Confidence Level

ECal Electromagnetic Calorimeters

EM Electromagnetic

EMB Electromagnetic Barrel Calorimeter

EMEC Electromagnetic End-Cap Calorimeter

FCal LAr Forward Calorimeter

GSC Global Sequential Calibration

HCal Hadronic Calorimeters

HLT High Level Trigger

HEC Hadronic End-Cap Calorimeter

ID Inner Detector

JES Jet Energy Scale

LO leading order

L1 Level-1 Trigger

LAr Liquid-Argon

LH likelihood

LHC Large Hadron Collider

LLH log likelihood

LLHR log likelihood ratio

MC Monte Carlo

MDT Monitored Drift Tube Chambers

NLO next-to-leading order

NNLO next-to-next-to-leading order

NP Nuisance Parameter

PDF Parton Distribution Functions

PE pseudo-experiments

PMT Photomultiplier Tubes

QCD Quantum Chromodynamics

RPC Resistive Plate Chambers

SCT Semi-Conductor Tracker

SPS Super Proton Synchrotron

TGC Thin Gap Chambers

TileCal Tile Barrel Hadronic Calorimeter

TRT Transition Radiation Tracker

SM Standard Model

ABSTRACT

This thesis presents a search for new resonances decaying to pairs of jets in 37 fb^{-1} of proton-proton collision data produced by the Large Hadron Collider at a center-of-mass energy of 13 TeV. The data was collected in 2015 and 2016 by the ATLAS detector. A new resonance search algorithm - SWIFT - was used to reduce the uncertainty in the data-driven estimate of the unknown backgrounds. SWIFT was utilized in a model-independent search, and also to perform model-dependent searches for excited quarks (q^*) and heavy gauge bosons (W'). No evidence for new phenomena was observed, so 95% confidence-level upper limits were calculated on the production rates of q^* and W'. Upper limits were also calculated for Gaussian models which represent first-order approximations for many theoretical models that predict new particles decaying to two jets.

CHAPTER 1

Introduction

A global effort of tens of thousands of scientists over the many past decades has made tremendous progress in understanding the subatomic particle world. The knowledge gained is synthesized into the *Standard Model of particle physics* which took its current form in late 1900s. Since then, the Standard Model (SM) and its predictions have been verified with great precision by a countless number of experiments. Despite the success of the theory, there are many reasons to believe that it is not complete, these include its inability to explain gravity (as a quantum-field theory), dark matter and dark energy[1]. Hence, new physics (in the form of new particles or interactions) must exist, though where and how it will appear is currently unknown. One of the best places to search for it is at the world's most powerful particle collider, the Large Hadron Collider (LHC).

The LHC is a proton-proton collider with a center-of-mass energy $\sqrt{s} = 13$ TeV. From each of its collisions, thousands of particles are created, most of which are produced from known SM processes and some of which might emerge from new physical interactions. This thesis will present a search for new physics from collision events that produce two jets - highly collimated sprays of particles. These are known as *dijet* events and are a powerful tool to search for new physics. The search is performed by looking for a localized excess above the smooth dijet *invariant mass* distribution pre-

[1]Dark matter and dark energy constitute approximately 95% of the total mass−energy content of the universe!

dicted by the SM (the *background*). The invariant mass provides a Lorentz-invariant measure of the energy of the two-jet system, and an excess in its distribution would signify the existence of a new particle with a definite invariant mass. The search is performed in a way that is sensitive to any new particle decaying to two jets, however, two specific new physics models are also evaluated: excited quarks (q^*) and heavy vector gauge bosons (W').

The data used in the search was collected using the ATLAS detector in the years 2015 and 2016 and amounts to a total integrated luminosity of 37 fb^{-1}. The most energetic dijet event recorded during this time period is shown in Figure 1.1 where the two back-to-back jets are clearly visible.

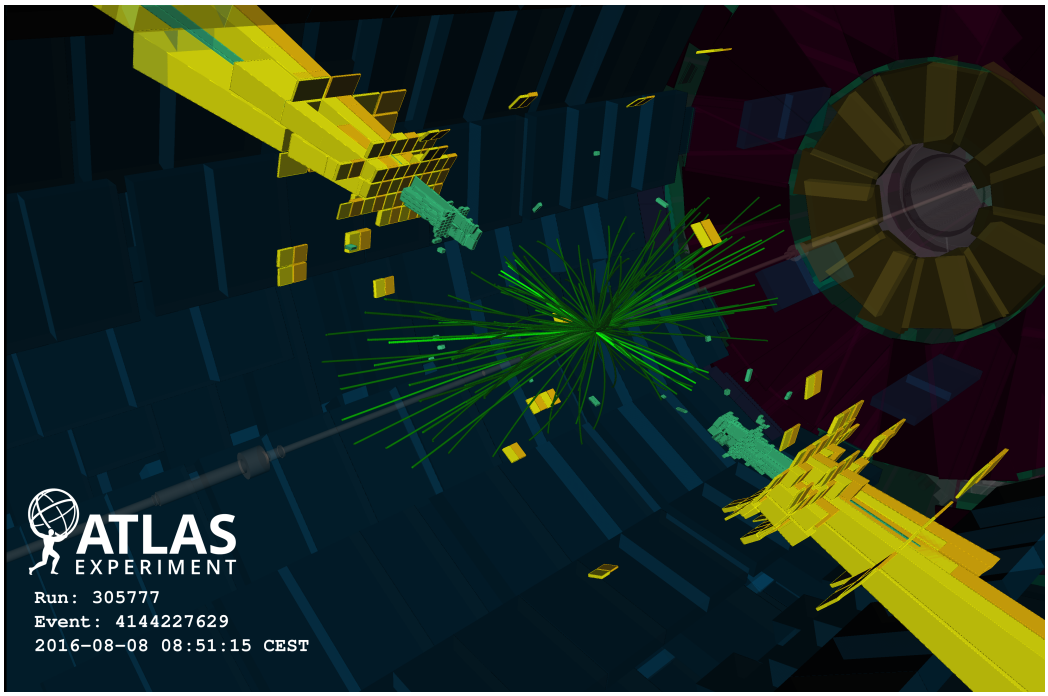

Figure 1.1: A visualization of the highest-mass dijet event, (Event 4144227629, Run 305777). This event has an invariant mass of 8.12 TeV. The green lines represent the tracks of the many particles emerging from the collision. The green and yellow towers represent the energy of the two jets and the tracks of the particles that create these energy sprays are also visible.

Traditionally, the background in dijet analyses has been modeled using a single parametric fit to the entire distribution. However, with increasing data this approach

becomes difficult, and a new method for modeling the background or conducting the search is required. This thesis presents a solution to this problem, the Sliding Window Fits (SWiFt) method. SWiFt conducts a resonance search in many small, overlapping and automatically sized windows - subranges of the full mass distribution. It also provides a background estimate over the full mass range by combining background estimates from all the windows. This allows the use of traditional bump-hunting tools that need a background model over the full data distribution.

This thesis is laid out in the following manner. Our current theoretical understanding of particle physics is outlined in Chapter 2. This provides a flavor of where particle physics stands today and why there is a need to look for new physical phenomena. Then, Chapter 3 discusses the experimental apparatus - the LHC and the ATLAS detector - used for the search. As the search is conducted in collisions that result in two jets, Chapter 4 details the general production, reconstruction and calibration of jets. Chapter 5 motivates the search for new physics in the dijet invariant mass distribution. It describes the SM dijet background and the new physics theories utilized in this thesis. Finally, past dijet analyses results are discussed. This chapter also introduces the traditional bump-hunting method used by ATLAS since 2010 and outlines the challenges with this approach. To address these challenges, Chapter 6 presents a new resonance search tool - SWiFt. The analysis selection and data quality are presented in Chapter 7 and the search results using SWiFt are shown in Chapter 8.

CHAPTER 2

The Standard Model of Particle Physics

As per our current understanding, there are four fundamental forces in nature. As shown in Table 2.1, these are the strong, electromagnetic, weak and gravitational forces. To each force is associated a particle that carries or transmits it. The strong force is carried by the gluons, the electromagnetic force is transmitted by the photons and the weak force is represented by the three massive vector bosons. Gravity is thought to be represented by the massless graviton, however, experimental evidence for such a particle is yet to be found.

Table 2.1: The four fundamental forces of nature with their relative strengths (for two protons in a nucleus) and ranges. The particles that carry these forces are also shown. With the exception of the hypothetical graviton, all the other carriers are well-measured and understood.

Forces	Strength	Range	Carriers
Strong	1	10^{-15}	Gluons g
Electromagnetic	10^{-2}	∞	Photons γ
Weak	10^{-6}	10^{-18}	Heavy gauge bosons $W^{\pm}, Z$
Gravitational	10^{-38}	∞	Gravitons G

Using these forces and their interactions with matter, all the visible interactions of the Universe can be described. A simple yet crucial example is the atom. An atom consists of a tiny nucleus, containing positively charged protons and electrically neutral neutrons. Surrounding the nucleus is a cloud of negatively charged electrons. The strong force is responsible for keeping the nucleus intact. It stabilizes the protons

and neutrons, keeping them bound to each other. The electromagnetic force binds the electron cloud to the nucleus, and the residual electromagnetic force then binds together atoms to create molecules. From molecules, via the interaction of chemistry comes all of biology and you, me and everything else exists! The weak force is responsible for radioactive decays and plays an important role in nuclear fission. Lastly, the gravitational force is responsible for aggregating atoms into large celestial bodies.

This chapter will open with a discussion of the theory of the Standard Model of particle physics. In the discussion, extra emphasis will be laid on the strong force as it leads to the production of jets, the subject of this thesis. Motivation for searching for new physics beyond the SM will also be provided.

2.1 The Standard Model of Particle Physics

The SM of particle physics is a mathematical theory that describes the interaction of three of the known fundamental forces (not the gravitational force) with the known fundamental matter particles, i.e. the *fermions*. These interactions occur via the exchange of force-carrying particles known as *gauge bosons*.

Fermions are spin-1/2 elementary particles that exist in three generations (as shown in Figure 2.1). They are divided into two groups: *quarks* and *leptons*. Each quark and lepton can exist in six flavors, each of which differs by mass and charges. The six flavors of quarks are called *up* (u), *charm* (c), *top* (t), *down* (d), *strange* (s) and *bottom* (b). The six lepton flavors are *electron* (e), *muon* (μ) and *tau* (τ), *electron neutrino* (ν_e), *muon neutrino* (ν_μ) and *tau neutrino* (ν_τ). For each of the fermions[1], there exists a corresponding anti-fermion with the same mass but reversed charges.

There are four spin-1 gauge bosons responsible for carrying the three forces: the massless *photon* (γ) gives rise to the electromagnetic force, the massless *gluons* (g)

[1]Except possibly the neutrinos.

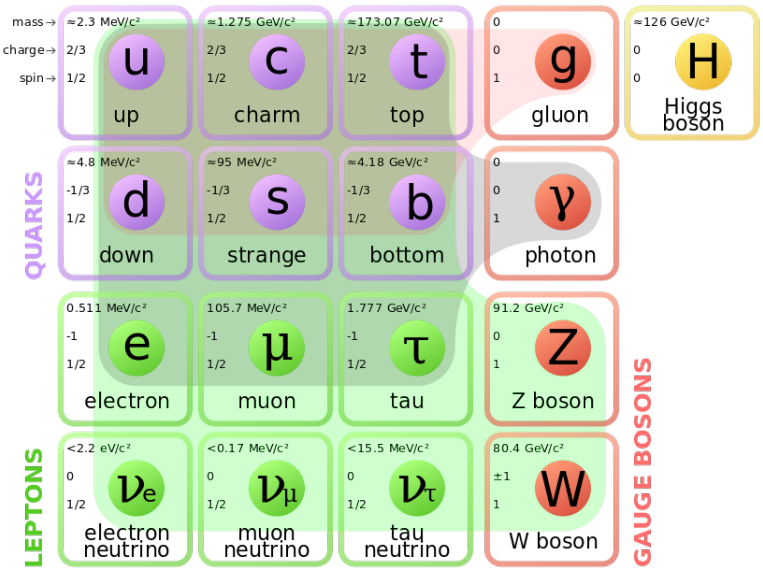

Figure 2.1: The fundamental particles in the Standard Model of particle physics [1]. The quarks and leptons are the matter particles and the gauge bosons are the carriers of the fundamental forces. The transparent green, grey and red boxes show the interactions of the weak, electromagnetic and strong forces, respectively. The last piece of the Standard Model to be found, the Higgs boson, is shown in the upper right corner.

create the strong force and the massive Z and W bosons carry the weak force. The last piece of the Standard Model is the spin-0 Higgs boson that was predicted to exist in the 1960s [42] [43] [44]. It is a quantum excitation of a fundamental spin-0 field, known as the Higgs field, that permeates the Universe. Due to the difficulty in producing and detecting the Higgs boson, its discovery by CERN in 2012 [45] [46] was a major experimental accomplishment.

Mathematically, the Standard Model is a relativistic quantum field theory that can be written as a product of the following symmetry groups

$$SU(3)_C \times SU(2)_L \times U(1)_Y \,. \tag{2.1}$$

Each group, also known as a gauge group, represents a set of transformations, which when applied to a physical system leaves it unchanged. $U(1)$ represents the group

of phase rotations on a single complex variable. $SU(2)$ and $SU(3)$ represent the groups of rotations on two and three complex variables, respectively. All experiments are consistent with the notion that these three internal symmetries are sufficient to explain the fundamental particles and their interactions. However, as to why nature obeys these symmetries and not any others is unknown. It is also remarkable to note that invariance under these abstract mathematical rotations leads to a complete description of the physical forces, particles and their interactions which can actually be measured in a laboratory. It is amazing that simple mathematical concepts underlie the complex world that we observe.

These transformations are *local*, i.e. they are space-time dependent transformations. The requirement of local gauge invariance *requires* the presence of vector fields that are associated with spin-1 vector bosons. These are the gauge bosons. Each symmetry group is also associated with a quantum number or charge; these charges are fundamental properties of the fermions. The non-Abelian analog of $U(1)_Y$ group's charge is called *weak hypercharge*, denoted by Y, and it has one gauge boson called B_μ (μ indexes the three space and one time dimension). The charge of the $SU(2)_L$ group is called *weak isospin*, denoted by T, and it has three gauge bosons called $W_\mu^{a=1,2,3}$. The subscript L stands for left as this symmetry is obeyed by left-handed fermions only. Finally, the $SU(3)_C$ group's charge is called *color* charge and it comes in three values: *red*, *green* and *blue*[2]. There are eight gauge bosons for this group called gluons and they are represented by $G_\mu^{a=1,2...,8}$.

The interaction of the gauge bosons with fermions, while conserving each symmetry group's charge, is what leads to the strong and *electroweak* forces (the latter is a combination of the electromagnetic and the weak force). It is once again remarkable to note that physical particles can be represented by pure mathematical constructs

[2]These names have nothing to do with the red, blue and green colors perceived by your eyes. They simply represent the three types of $SU(3)$ charges, and could have also been called Mothra, Simon and Wilson.

- gauge bosons being square, unitary matrices with determinant one and fermions being column matrices.

2.1.1 The Electroweak Interaction

All particles have the $U(1)$ and $SU(2)$ gauge invariances, the gauge bosons for which are the B_μ and the three $W_\mu^{a=1,2,3}$, respectively. However, there is a difference in the way these symmetries are manifested in nature: whereas all fermions contain the $U(1)$ hypercharge Y, only pairs of left-handed fermions, called doublets, transform under the $SU(2)$ weak isospin, T. The right-handed fermions (e_R, μ_R, τ_R) are electroweak singlets. The left-handed fermion doublets are:

$$\begin{pmatrix} \nu_e \\ e \end{pmatrix}_L , \begin{pmatrix} \nu_\mu \\ \mu \end{pmatrix}_L , \begin{pmatrix} \nu_\tau \\ \tau \end{pmatrix}_L , \begin{pmatrix} u \\ d \end{pmatrix}_L , \begin{pmatrix} c \\ s \end{pmatrix}_L , \begin{pmatrix} t \\ b \end{pmatrix}_L . \tag{2.2}$$

Rotations in $SU(2)$ space can transform each 'up' element of the doublet into the 'bottom' element, e.g. ν_e transforms to e, u transforms to d, etc. These rotations are brought about by the two (out of four) physical gauge bosons of the unified $U(1) \times SU(2)$ electroweak force: W^+ and W^-. The interaction of these two bosons in addition to the interactions with the neutral Z boson with the left-handed fermion doublets creates the weak force. The fourth physical gauge boson is the photon (γ), which is responsible for the electromagnetic force. The physical gauge bosons of the

electoweak force are written as a combination of the B_μ and $W_\mu^{a=1,2,3}$ bosons:

$$W^+ = (W_\mu^1 - iW_\mu^2)/\sqrt{2} \tag{2.3}$$

$$\begin{aligned} W^- &= (W_\mu^1 + iW_\mu^2)/\sqrt{2} \\ Z &= \cos\theta_W \cdot W_\mu^3 - \sin\theta_W \cdot B_\mu \\ \gamma &= \sin\theta_W \cdot W_\mu^3 + \cos\theta_W \cdot B_\mu \,. \end{aligned} \tag{2.4}$$

Here θ_W is the weak mixing angle. It specifies the rotation angle of the W_μ^3 and B_μ states, as a result producing the Z and the γ.

Since the photon is a mixture of W_μ^3 and B_μ, the electric charge, denoted by Q, is a combination of the $U(1)$ and $SU(2)$ charges

$$Q = T_3 + \frac{Y}{2}, \tag{2.5}$$

where T_3 is the third component of the weak isospin charge. Particles with non-zero electric charge interact with the photon. Table 2.2 summarizes the charges of the electroweak sector. Notice that there are no right-handed neutrinos in the table. Either they do not exist, or if they do, they are either too heavy or too weakly interacting to be produced and detected in accelerators.

The fundamental interactions allowed by the electroweak force are shown by the Feynman diagrams in Figure 2.2. Feynman diagrams are pictorial representations of particle interactions. They provide a simple visualization of complicated particle physics formulae and thus help in simplifying complex calculations. Each line in the diagram represents a particle (fermion or boson) and point of convergence of these lines is called a vertex which is characterized by a coupling strength. Figure 2.2 (a) shows the basic Feynman diagram for the electromagnetic interaction, the vertex of

Table 2.2: The charges of the electroweak force. Y represents the $U(1)$ hypercharge, T_3 stands for the third component of the $SU(2)$ weak isospin charge and Q is the electromagnetic charge.

	Generations			Electro-weak Charges		
	I	II	III	Y	T_3	Q
Quarks	u_L	c_L	t_L	1/3	1/2	2/3
	d_L	s_L	b_L	1/3	-1/2	-1/3
	u_R	c_R	t_R	4/3	0	2/3
	d_R	s_R	b_R	-2/3	0	-1/3
Leptons	ν_{eL}	$\nu_{\mu L}$	$\nu_{\tau L}$	-1	-1/2	0
	e_L	μ_L	τ_L	-1	1/2	-1
	e_R	μ_R	τ_R	-2	0	-1

which is characterized by the coupling constant $\alpha = 1/137$ (at low q^2). The remaining diagrams show the interactions of the weak force, characterized by the coupling constant $\alpha_W = 1/30$ (at low q^2). The last six diagrams show the interaction amongst the gauge bosons. These interactions are allowed as the bosons carry electroweak charges themselves. The W^+ and W^- have an electric charge of +1 and -1, respectively, and all three W^+, W^-, Z carry weak isospin. The Z and γ are electrically neutral and they are both mixed states of W^3_μ and B_μ. For each interaction where photons can be exchanged, Z bosons can be exchanged as well. However, the opposite does not always work - Z bosons can interact with neutrinos, however, photons do not.

Unlike the photon and the gluons, the bosons of the weak force, W^+, W^- and Z, are massive. This is why the weak force is short-ranged (and hence is called weak). The masses of the weak gauge bosons cannot be described by simply adding mass terms to the Lagrangian[3]. This is because the added mass terms break the local gauge invariance of the SU(2) symmetry. Hence, a mechanism that preserves local invariance while giving mass to the weak bosons is required. The mechanism that does so is known as the *Higgs mechanism* and this, in conjunction with the process

[3]The Lagrangian is a quantity that describes the state of a physical system. It is the kinetic energy minus the potential energy of the system.

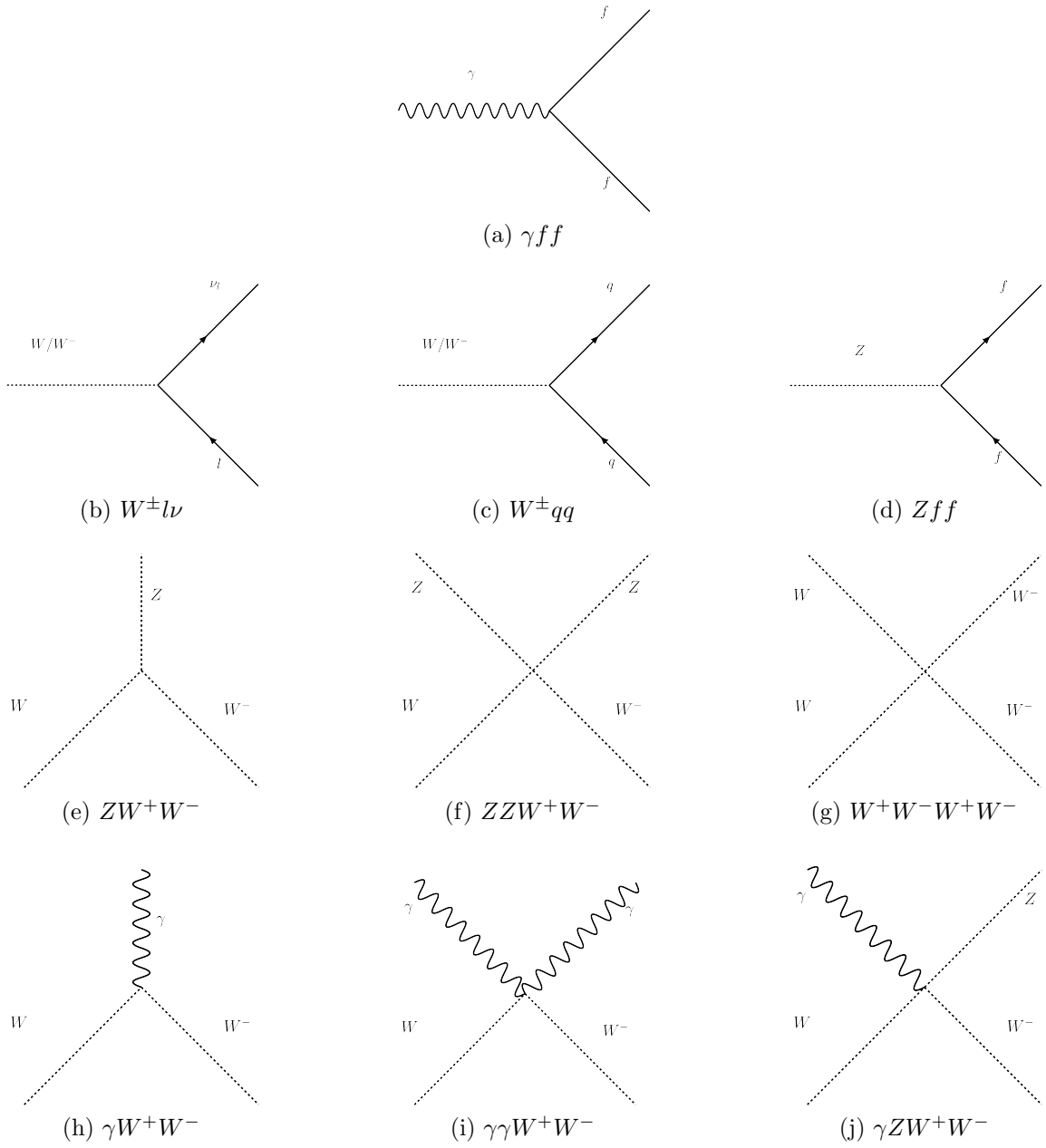

(a) γff (b) $W^{\pm}l\nu$ (c) $W^{\pm}qq$ (d) Zff

(e) ZW^+W^- (f) ZZW^+W^- (g) $W^+W^-W^+W^-$

(h) γW^+W^- (i) $\gamma\gamma W^+W^-$ (j) γZW^+W^-

Figure 2.2: Feynman diagrams for the basic interactions allowed by the electroweak force. The wavy lines represent photons, the dotted lines show the $W^{\pm}$, Z bosons, and the solid lines represent fermions. (a) The electromagnetic interaction, where f can be any fermion except neutrinos. (b), (c), (d) represent the interactions of the weak force, where the Z boson interacts with all fermions. Diagrams (e) and up show the interactions between the bosons themselves.

of electroweak unification, is known as *spontaneous electroweak symmetry breaking*.

2.1.2 Spontaneous Electroweak Symmetry Breaking

Spontaneous electroweak symmetry breaking is the process responsible for explaining the masses of the W/Z bosons. In fact, the same mechanism is also responsible for giving mass to the fermions. During this process, the $SU(2)_L \times U(1)_Y$ symmetry (corresponding to the electroweak force) is broken, leaving behind a $U(1)$ symmetry (corresponding to the electromagnetic force) with a massless photon γ and three massive gauge bosons; the W^+, W^- and Z. The process supposes a complex, scalar (spin-0) field, known as the Higgs field ϕ, which is a doublet in $SU(2)$ space and carries non-zero hypercharge. The field's Lagrangian $\mathcal{L}$ is invariant under local gauge transformations

$$\begin{aligned} \mathcal{L} &= T - V \\ &= (\partial_\mu \phi)^\dagger (\partial^\mu \phi) - (\mu^2 \phi^\dagger \phi + \lambda (\phi^\dagger \phi)^2) \,, \end{aligned} \tag{2.6}$$

where T is the kinetic energy and V is the potential energy (also known as the interaction term). If the field exists in the universe, its symmetry is spontaneously broken. This is a result of the interplay of the two self-interaction terms: the $\phi^\dagger\phi$ and $(\phi^\dagger\phi)^2$ terms. If $\mu^2 > 0$ and $\lambda > 0$, the potential, as a function of the field, has a minimum at zero and no symmetry breaking occurs - the minimum is at the point of symmetry. For $\mu^2 < 0$ and $\lambda > 0$, the potential as a function of the field is the *mexican hat potential*, Figure 2.3. The minimum acquires a non-zero value, called the *vacuum expectation value* (vev), along the circle at the base of the potential. The vev is a measure of the vacuum energy density of the universe and its value of 246 GeV signifies the existence of a Higgs field in empty space! The particles associated with the field manifest as small perturbations around the minimum, where the original

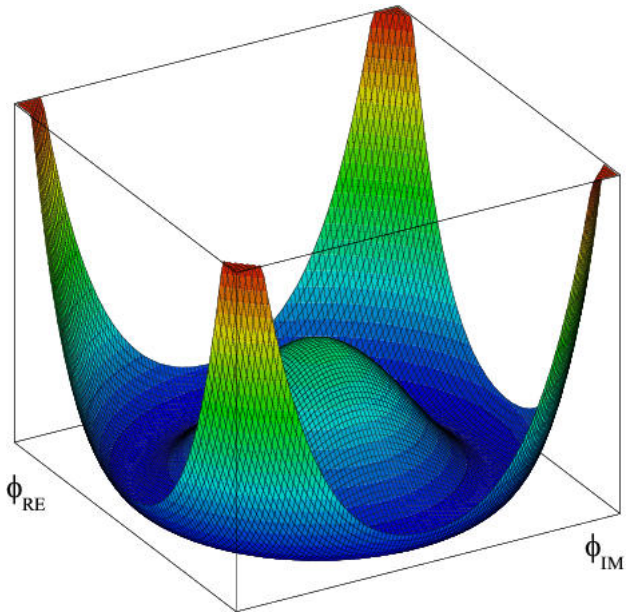

Figure 2.3: Higgs potential in two dimensions. [2].

symmetry of the Lagrangian is hidden. Three (of the four) excitations of the Higgs field become the longitudinal components of the W^+, W^-, Z bosons, hence making them massive. After symmetry breaking, a $U(1)$ symmetry remains. This is the electromagnetic force with its massless boson, the photon. The fourth excitation of the Higgs field remains unabsorbed and is known as the Higgs boson.

Since the universe is filled with the Higgs field with non-zero vev, fermions gain their masses by interacting with it. More specifically, the Higgs field couples the left- and right-handed fermions, and the strength of this coupling provides their masses.

2.1.3 The Strong Interaction

Quarks carry the $SU(3)$ color charge and interact with each other via the exchange of massless gluons. This interaction is the strong force, the study of which is known as Quantum Chromodynamics (QCD). Each quark can be either red (r), green (g) or blue (b) and each anti-quark can be anti-red ($\bar{r}$), anti-green ($\bar{g}$) or anti-blue ($\bar{b}$). Each gluon carries one unit of color and one unit of anti-color. As the gluons carry

color, they can interact amongst themselves.

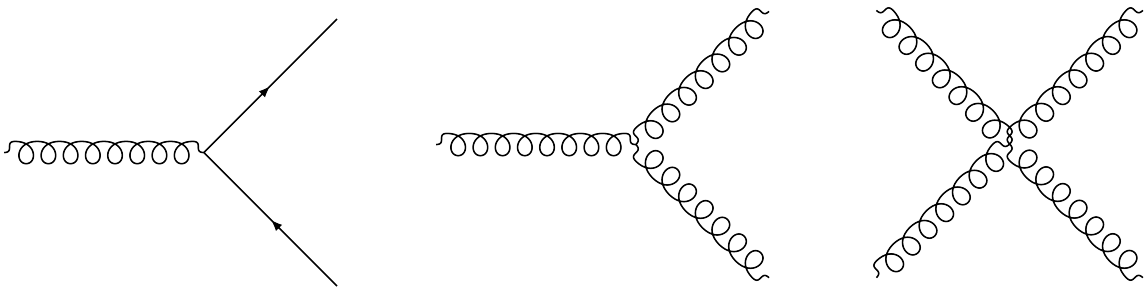

(a) gqq (b) ggg (c) gggg

Figure 2.4: Feynman diagrams for the basic interactions allowed by QCD. The curling lines represent gluons and the straight lines show quarks. (a) Interaction where a quark emits/absorbs a gluon, (b) gluon splitting into two gluons and (c) four-point gluon self-interaction.

The basic interactions allowed by QCD are shown by the Feynman diagrams in Figure 2.4. The vertex of each diagram is characterized by the strong coupling constant α_S. At a particular four-momentum[4] transfer of Q^2, it can be written as

$$\alpha_s(Q^2) = \frac{1}{b_0 \ln(Q^2/\Lambda^2_{QCD})}\,, \tag{2.7}$$

where $b_0 = (11n_c - 2n_f)/12\pi$, Λ^2_{QCD} is the QCD energy scale (around 200 MeV) and n_c and n_f are the numbers of color and quark flavors, respectively. For $Q^2 < \Lambda^2_{QCD}$, bound quark states exist. At high Q^2 ($>> \Lambda^2_{QCD}$), the QCD coupling decreases logarithmically as shown in Figure 2.5. This is known as the "running" of the coupling and it leads to asymptotic freedom - at high-energy, the coupling between quarks and gluons weakens and, as a consequence, they behave almost as free particles. This is the region where perturbative QCD can be used.

The predictions of QCD (above Λ^2_{QCD}) the are computed perturbatively, i.e. using a power-series expansion in the coupling constant. The first term in this expansion -

[4]Four-momentum is the generalization of the three-dimensional momentum to the four-dimensional spacetime, i.e. $P = (E/c, p_x, p_y, p_z)$. E is the energy of the particle and (p_x, p_y, p_z) is its momentum.

leading order (LO) prediction - is used as the simplest model of QCD's effects. LO predictions can be represented using Feynman diagrams with $\mathcal{O}(\alpha_S^2)$, i.e. consisting of two vertices. These diagrams represent the scattering of two particles (a $2 \rightarrow 2$ interaction). Expansions with the first two powers of the coupling are called next-to-leading order (NLO), expansions with the first three are called next-to-next-to-leading order (NNLO), etc. Each provides a more refined prediction of QCD's effects than the last. Feynman diagrams representing NLO interactions are of $\mathcal{O}(\alpha_S^3)$ with three vertices. Examples of such an interaction would be the emission of a quark or gluon after a two body scattering event, i.e. a $2 \rightarrow 3$ interaction.

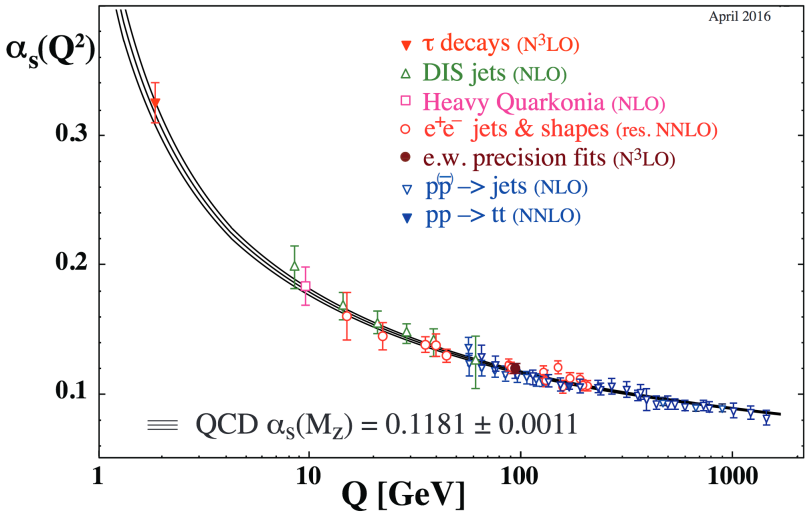

Figure 2.5: Measurement of the strong coupling constant, α_s as a function of energy scale Q. The respective degree of QCD perturbation theory used in the extraction of α_s is indicated in brackets (NLO: next-to-leading order; NNLO: next-to-next-to leading order; res. NNLO: NNLO matched with resummed next-to-leading logs; N3LO: next-to-NNLO) [3].

The strong force is responsible for creating colorless quark bound states known as hadrons. Each hadron comprises of two or three valance quarks bound to each other via the exchange of gluons. The bound quarks exist in a virtual sea of non-valance quarks and gluons. The two-quark hadrons are known as *mesons* and they always contains a color/anti-color quark set. On the other hand, the three-quark hadrons are

know as *baryons* and they contain a red/blue/green set of quarks. The combination of color/anti-color and red/blue/green quarks is what makes the hadrons colorless. Out of the vast number of hadrons, the most familiar and the only stable ones are the proton (uud) and neutron (udd) (technically, a neutron is only stable inside a nucleus. A free neutron decays in approximately 13 minutes). All the other hadrons are created by cosmic rays or particle accelerators. Being highly unstable, they decay within a range of 10^{-24} to 10^{-8} seconds.

Isolated quarks are never observed. This is due to the property of *color confinement*. This property arises due the linear increase in potential energy of two quarks with increasing distance between them. It would take an infinite supply off energy to separate them and hence they remain confined within hadrons. If the quarks are forced apart (for example, by energetic pp collisions), they fragment into multiple hadrons and the fragmentation continues until all of the collision energy is exhausted. This leads to the production of conical sprays of particles known as *jets*.

2.2 The Parton Model and The Hadronic Jet Production

Jets are conical sprays of colorless hadrons that are ubiquitously produced during high energy hadron-hadron collisions. They are an inevitable consequence of asymptotic freedom and color confinement. Jets are easy to identify in detectors and play an important role in searching for new physics. In high energy hadron-hadron collisions (e.g. proton-proton collisions), they are produced by the direct interaction of *partons* (the quarks and gluons of the colliding hadrons) in three consecutive steps: hard scattering, parton showering and hadronization. Figure 2.6 shows a schematic view of this process.

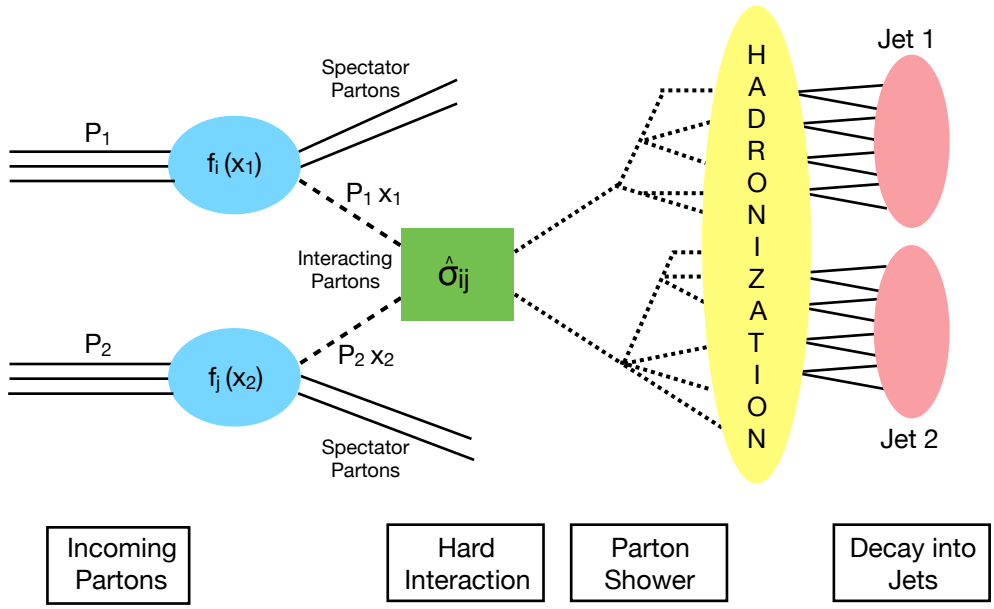

Figure 2.6: Creation of jets from hard scattering of hadrons.

2.2.1 Parton Distribution Functions and the Hard Scatter

The incoming hadrons, with four-momenta P_1 and P_2, contain various valence and sea partons. The partons possess varying fractions of the hadrons momentum, the distribution of which is given by the Parton Distribution Functions (PDF). At a momentum scale μ^2, they describe the probability that a parton will carry a specific fraction of the hadrons momentum, x. They are extracted by fitting deep inelastic lepton-nucleon scattering data and are shown for two momentum scales ($\mu^2 = 10$ and 10^4 GeV^2) in Figure 2.7.

When two highly energetic partons (of types i and j) interact with each other (carrying momenta $p_1 = x_1 P_1$, $p_2 = x_2 P_2$, respectively), they produce an interaction known as a *hard scatter*. The probability of such an interaction, known as the *cross-section*, is given by $\hat{\sigma_{ij}}$ and is calculated using perturbative QCD. The total cross-section for the collision process is given by integrating over all possible initial state

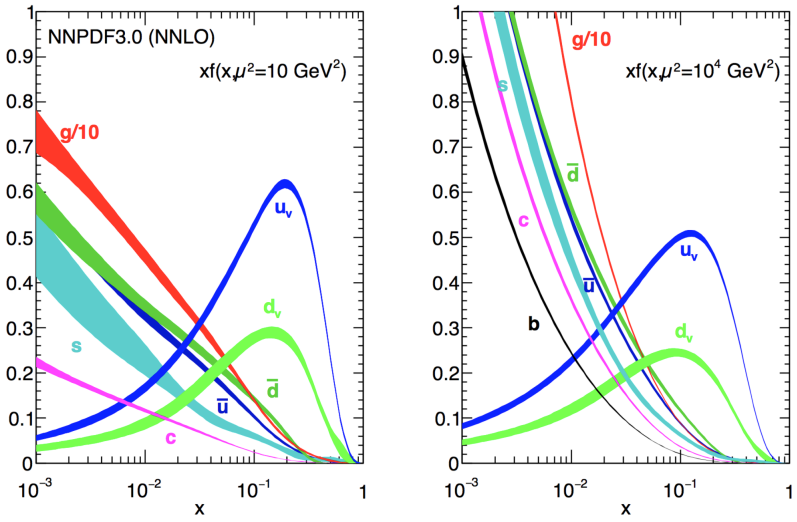

Figure 2.7: Parton Distribution Functions [3] obtained in NNLO NNPDF3.0 global analysis [4] at scales $\mu^2 = 10$ GeV^2 (left) and $\mu^2 = 10^4$ GeV^2 (right).

momenta for i and j weighted according to their PDF functions $f_i(x_1)$ and $f_j(x_2)$

$$\boldsymbol{\sigma}(P_1, P_2) = \sum_{i,j} \int dx_1 dx_2 f_i(x_1, \mu_F^2) f_j(x_2, \mu_F^2)\ \hat{\sigma}_{ij}(p_1, p_2, \alpha_S(\mu_F^2), Q^2/\mu_F^2)\,, \qquad (2.8)$$

where Q denotes the characteristic scale of the hard scattering and μ_F represents the factorization scale. The factorization scale separates the "long" and "short" distance physics. A parton with a transverse momentum less than μ_F is considered to be a part of the hadron and does not contribute to σ_{ij}. On the other hand, partons with transverse momenta larger than μ_F are part of σ_{ij} and contribute to the hard scatter. The non-interacting partons are known as the *spectator partons* as they do not participate in the hard scattering interaction.

2.2.2 Parton Shower

After the energetic hard interaction, violently accelerated partons are created. Just as highly accelerated electric charge produces electromagnetic radiation, highly energetic colored partons will create QCD radiation by emitting gluons. As gluons themselves

carry color charge, they radiate more gluons until the energy of the hard scatter is exhausted, leading to *parton showers*.

2.2.3 Hadronization

At the end of the showers, the parton energies reduce enough (down to ~ 1 GeV) for the strong confining color force to dominate, as a result of which hadrons are formed. This process is known as *hadronization*. The theory of the process of hadronization is not fully understood (as it cannot be treated perturbatively), however, is can be successfully described by a few models that rely on general features of QCD. One of them (which is also used in the simulation of jet events in the analysis presented in this thesis) is the string model [47]. It is based on the observation that at large distances, as the color sources (suppose quark-antiquark pair) separate, their potential energy increases linearly. This is thought to be so because of a gluon string connecting the quark-antiquark pair. When the potential energy becomes of the order of the mass of the quarks, the string snaps, creating a new quark-antiquark pair. The original quark combines with the new anti-quark and the original anti-quark combines with the new quark. The two new pairs of quark-antiquark separate and split into four pairs and this process repeats itself a large number of times. At the end, many new mesons and baryons are created. The collection of these hadrons, traversing through detectors, are then identified as jets.

2.3 Beyond the Standard Model

The Standard Model of particle physics discussed in the previous sections is a very successful theory and over the past decades, its predictions have been verified by experiment over and over again. It provides us with a sound understanding of the fundamental forces, particles and their interactions. Despite its success, there are a

number of questions it provides no answers to, such as: why do fermions come in such different flavors and masses, why does the weak force operate on left-handed doublets only, why are all the parameters of the theory so specific (so *finely tuned*), why is gravity so weak as compared to the other forces and how does it fit into the Standard Model, and why is there more matter than anti-matter in the universe? These questions seem to imply that perhaps the Standard Model is a low-energy approximation of a more general theory. There is also mounting experimental evidence from cosmology - the existence of dark matter [48] and dark energy [49] - that suggest the existence of new physics.

Many of the theories that attempt to solve these problems predict the existence of new particles. If the masses of these particles are within the reach of the LHC, they might appear in its proton-proton collisions. In particular, if they interact strongly, i.e. via quarks and gluons, they would decay strongly to quarks and gluons as well. The decaying particles would appear as jets in the detectors of the LHC. This makes events with two jets the first and simplest state to search. Some new particles/states that are predicted to decay into two jet and appear as resonances in the dijet invariant mass distribution are excited quarks and new heavy gauge bosons. This thesis presents a search for excited quarks and heavy gauge bosons that decay to two jets. The details of the theories that predict these particles as well as the simulation of their experimental signatures are discussed in Chapters 8 and 5 respectively. To lowest-order, many new physics models can be roughly approximated with a Gaussian shape. Thus, results using a variety of Gaussian shapes are also shown. Some of the search results presented in this thesis were published in Ref. [50].

CHAPTER 3

The Experiment

The Large Hadron Collider (LHC) and its experiments are the end result of decades of research and development by thousands of scientists and engineers from all over the world. The data analyzed in this thesis was collected by the ATLAS detector. This chapter will describe the LHC accelerator complex as well as the ATLAS detector.

3.1 The Large Hadron Collider

The LHC [51] is a circular proton-proton accelerator that sits in a 3.8 m wide concrete-lined tunnel, 100 m below the French and Swiss border. It is 27 km in circumference and consists of superconducting magnets that are designed to accelerate proton beams to energies of 7 TeV[1]. Due to a magnetic quench accident in 2008 [52], the beam energies are set to 6.5 TeV.

The LHC is the last stage of a complex chain of machines that accelerate particles to increasingly higher energies, Figure 3.1. Starting from a simple bottle of hydrogen, the accelerator complex creates highly energetic beams of protons. The steps involved in this are discussed next. Protons are obtained from a bottle containing hydrogen gas by stripping away electrons using an electric field. They are accelerated to an energy of 50 MeV by the first accelerator in the chain, Linac 2, which uses radio frequency cavities, with alternating positive and negative charge, to accelerate

[1]This corresponds to a speed of 99.9999991% times the speed of light.

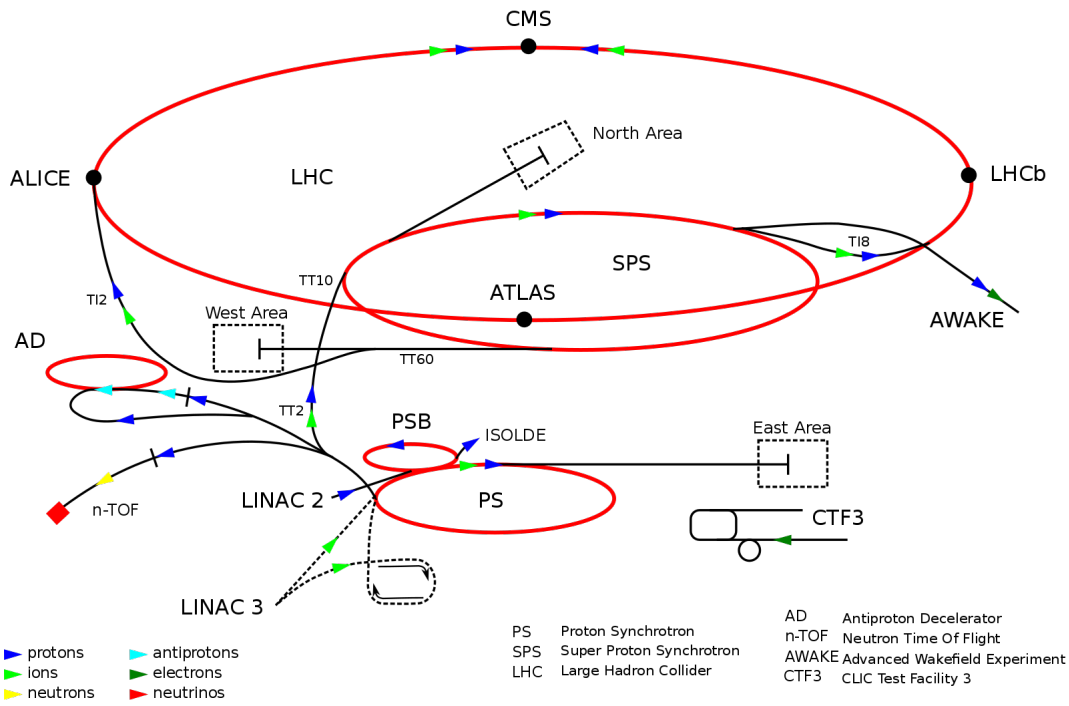

Figure 3.1: The CERN Accelerator Complex. The LHC is the last ring (the largest circle) in a set of complex accelerators [5].

the protons. The beam is then injected into the Proton Synchrotron Booster (PSB), which boosts the protons to 1.4 GeV. Next, the beam is injected into the Proton Synchrotron (PS), which accelerates the protons to 25 GeV, followed by the Super Proton Synchrotron (SPS) where they are accelerated to 450 GeV. The PS has 277 conventional electromagnets, including 100 dipole magnets to bend the beams around the ring. The SPS has 1317 conventional electromagnets, including 744 dipole magnets. Before the LHC, it was Center of European Nuclear Research (CERN)'s most powerful proton accelerator and it collided protons and anti-protons. In 1983, the W and Z bosons were discovered by the UA1 [53] [54] and UA2 [55] [56] collaborations from the data collected using the SPS. Finally, the beams are injected into the LHC (one traveling clockwise and the other counter-clockwise) and proton-proton collisions occur at a frequency of 40 MHz (every 25 ns). The peak *instantaneous luminosity* of the beams is a staggering 10^{34} cm^{-2}s^{-1}. Instantaneous luminosity measures how

many protons can be squeezed in a given space in a given time and is proportional to the number of collisions. It is defined as

$$\mathcal{L} = k_b N_b^2 f_{\text{rev}} \frac{\gamma F}{4\pi \epsilon_n \beta^*} \,, \tag{3.1}$$

where k_b is the number of bunches per ring, N_b is the number of protons per bunch and f_{rev} is the revolution frequency of 11.2 kHz. γ is the relativistic factor for the protons and ϵ_n is the normalized RMS transverse beam emittance. β^* is the beta-function at the interaction point. It corresponds to the narrowness of the beam and depends on the focusing magnets. F is a geometric reduction factor that accounts for the loss in luminosity due to the crossing angle of the beams.

The instantaneous luminosity is integrated over time to obtain the *integrated luminosity* ($\int \mathcal{L} dt$) with units of inverse barns. Typically inverse femtobarns are used where 1 femtobarn (fb) = 10^{-39}cm^2. The integrated luminosity is related to the collision cross-section (σ_{events}) by

$$\int \mathcal{L} dt = \frac{N_{\text{events}}}{\sigma_{\text{events}}} \,, \tag{3.2}$$

where N_{events} is the number of events. For example, 1 fb^{-1} integrated luminosity corresponds to 1 event per femtobarn of cross-section in the data.

Due to the radio frequency acceleration, the proton beams are not continuous. They are designed to have $2,808$ bunches where each bunch contains 1.15×10^{11} protons spread over a length of approximately 30 cm. The bunches are separated by 7.5 m or 25 ns.

It takes 4 minutes and 20 seconds to fill the LHC ring starting from the hydrogen gas. Once in the LHC, each beam reaches a maximum energy of 6.5 TeV after 20 minutes of circulation. After stable beams are achieved, collisions occur (with a center-of-mass energy of 13 TeV) at four interaction points (IP), each housing a dif-

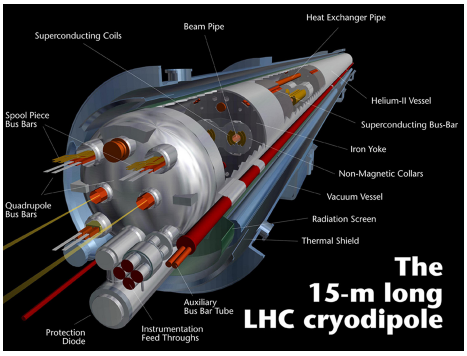

(a) Superconductor Dipole

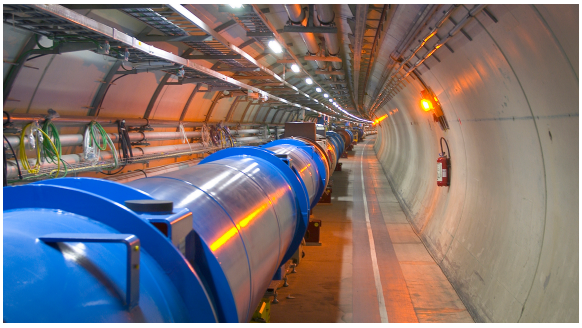

(b) LHC Tunnel

Figure 3.2: (a) A cross-section of the superconducting dipole magnet is shown [6] and (b) a string of these magnets can be seen in the LHC tunnel [7].

ferent particle detector: ATLAS [9], ALICE [57], CMS [58] and LHCb [59]. Collisions continue for roughly 24 hours. Once the bunches lose 50% of their protons, the LHC is injected with new beams.

The LHC is mainly made of vacuum-sealed pipes (104 km), vacuum systems, cryogenics and lot of magnets (total of $9,593$). The beams are focused by using 392 main quadpole magnets and steered by using $1,232$ superconducting dipole electromagnets made of niobium-titanium (NbTi) cables. The dipole magnets are 15 m long and weigh around 35 tons each. They draw a current of $11,850$ A, generate a magnetic field of 8.33 T, and are kept at a temperature of 1.9 K (271.3 C)[2]. This temperature is reached by pumping liquid helium from the cryogenics system into the magnet systems. The LHC cryogenics system is the largest and coldest cryogenics system in the world. It uses 120 tons of gaseous helium and $10,000$ tons of liquid helium to cool $4,700$ tons of material. The 54 km of piping that makes the two beam pipes (carrying the two proton beams in opposite directions) are kept at ultra-high vacuum: 10^{-10} to 10^{-11} mbar[3].

[2]This temperature is colder than the temperature of outer space: 2.7 K or 270.5 C.
[3]This is equivalent to vacuum found on the surface of the Moon.

3.1.1 Running Conditions in 2015 and 2016

In 2015 and 2016, the LHC operated at a center-of-mass energy of 13 TeV. The total integrated luminosity delivered was 42.7 fb^{-1}, which is twice the amount collected at $\sqrt{s} = 8$ TeV.

In 2015, an integrated luminosity of 4.2 fb^{-1} was delivered with a peak instantaneous luminosity of 5.02×10^{33} $\text{cm}^{-2}\text{s}^{-1}$. The ATLAS detector successfully recorded 3.9 fb^{-1}. With bunches colliding every 25 ns, the average number of collision events per bunch crossing was 13.7. Out of the multiple pairs of protons colliding in bunch crossing, only one pair contains the interesting hard scattering event. The remaining collisions create a background which is know as *pileup*. There are two kinds of pileup: in-time and out-of-time pileup. The former represents the number of collisions in each bunch crossing and the latter is the number of collisions coming from the previous bunch crossing.

In 2016, the LHC's performance was outstanding - it delivered 60% more data than predicted. The data collected was more than the sum of data collected in 2012 and 2015. It delivered an integrated luminosity of 38.5 fb^{-1}, out of which ATLAS recorded 35.6 fb^{-1}. The peak instantaneous luminosity was 1.38×10^{34} $\text{cm}^{-2}\text{s}^{-1}$ with an average of 24.9 collisions per bunch crossing.

Figure 3.3 shows the 2015 and 2016 run conditions as a function of time for the ATLAS detector: the total integrated luminosity, the peak luminosity and the peak interaction per bunch crossing. Figure 3.4 shows the pileup condition for the two years.

3.2 The ATLAS Detector

A Toroidal LHC ApparatuS (ATLAS) is a general purpose, hermetically-sealed detector that records the results of LHC's proton-proton collisions. It provides nearly full

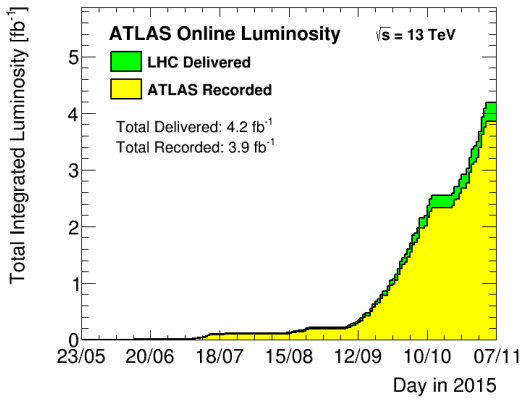

(a) 2015 Integrated Luminosity

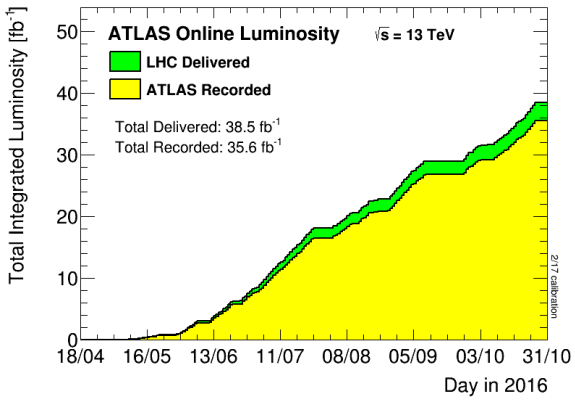

(b) 2016 Integrated Luminosity

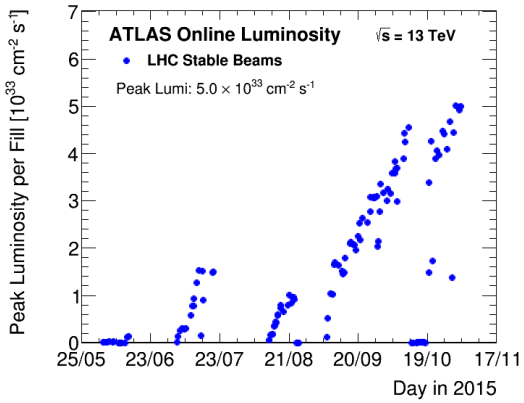

(c) 2015 Peak Luminosity

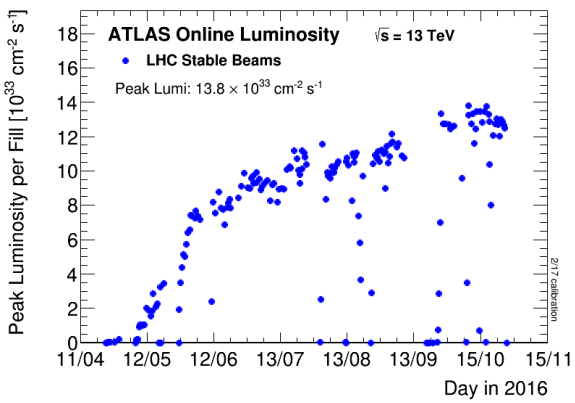

(d) 2016 Peak Luminosity

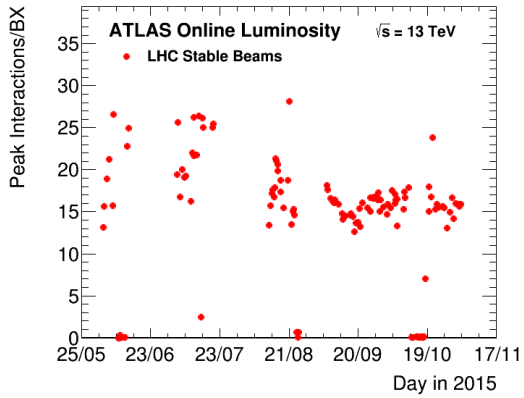

(e) 2015 Peak Interaction/bunch crossing

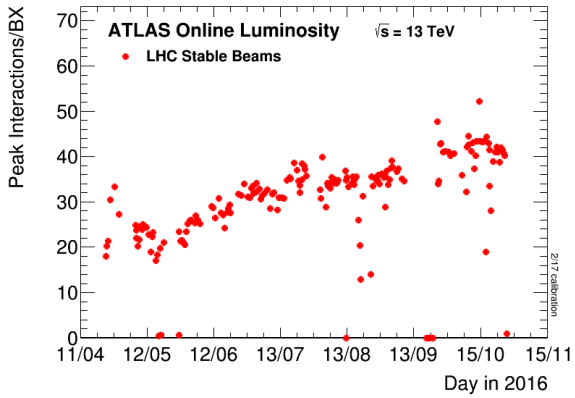

(f) 2016 Peak Interaction/bunch crossing

Figure 3.3: The LHC run conditions as a function of time as seen by the ATLAS detector for 2015 and 2016 [8]. (a), (b) show the integrated luminosity. (c), (d) show the peak luminosity per beam injection into the LHC. (e), (f) show the peak interaction per bunch crossing.

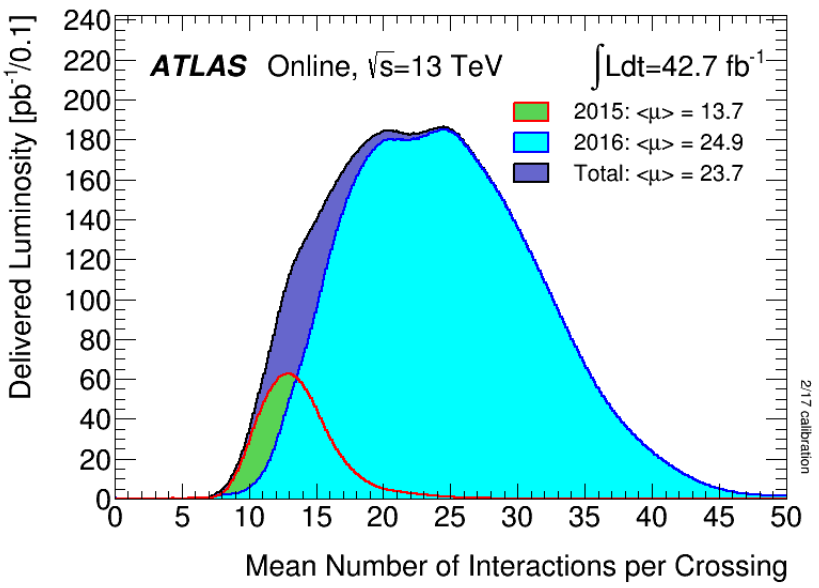

Figure 3.4: Pileup condition for 2015 and 2016 [8]. The plot shows the delivered luminosity as a function of average interactions per bunch crossing.

azimuthal coverage and is designed to reconstruct particles produced during collisions. In total, it weights 7000 tons and is 44 m long with a diameter of 25 m.

The coordinates and orientation of ATLAS are described using a right-handed coordinate system centered at the nominal collision point. The beam pipe defines the z-axis, the positive x-axis points to the center of the LHC ring and the positive y-axis points upwards. The azimuthal angle ϕ is measured from the x-axis in the x-y plane perpendicular to the z-axis. The polar angle θ is the angle from the z-axis. A more useful way of defining the polar angle, to describe detector coordinates as well as coordinates of a particle moving relative to the beam axis, is the pseudorapidity η. It is defined as

$$\eta = -\ln\left[\tan\left(\frac{\theta}{2}\right)\right] = \frac{1}{2}\ln\left(\frac{|\vec{p}| + p_z}{|\vec{p}| - p_z}\right), \tag{3.3}$$

where $\vec{p}$ is the three-momentum and p_z is the longitudinal momentum of a moving particle. In the case of massive objects traveling very close to the speed of light, the

pseudorapidity converges to the rapidity y which is defined as:

$$y = \frac{1}{2} \ln \left(\frac{E + p_z}{E - p_z} \right) , \tag{3.4}$$

where E is the energy of the object. The transverse momentum p_{T} and transverse energy E_{T} of the object are defined in the x-y plane and are perpendicular to p_z. The distance ΔR in the pseudorapidity-azimuthal space is defined as:

$$\Delta R = \sqrt{\Delta\eta^2 + \Delta\phi^2} . \tag{3.5}$$

ATLAS is composed of several subdetector and magnet systems that sit concentrically around the beam pipe (Figure 3.5). The main subdetectors are the inner tracker, the electromagnetic calorimeter, the hadronic calorimeter, and the muon spectrometer. The main magnet systems are the central solenoid and the barrel toroid.

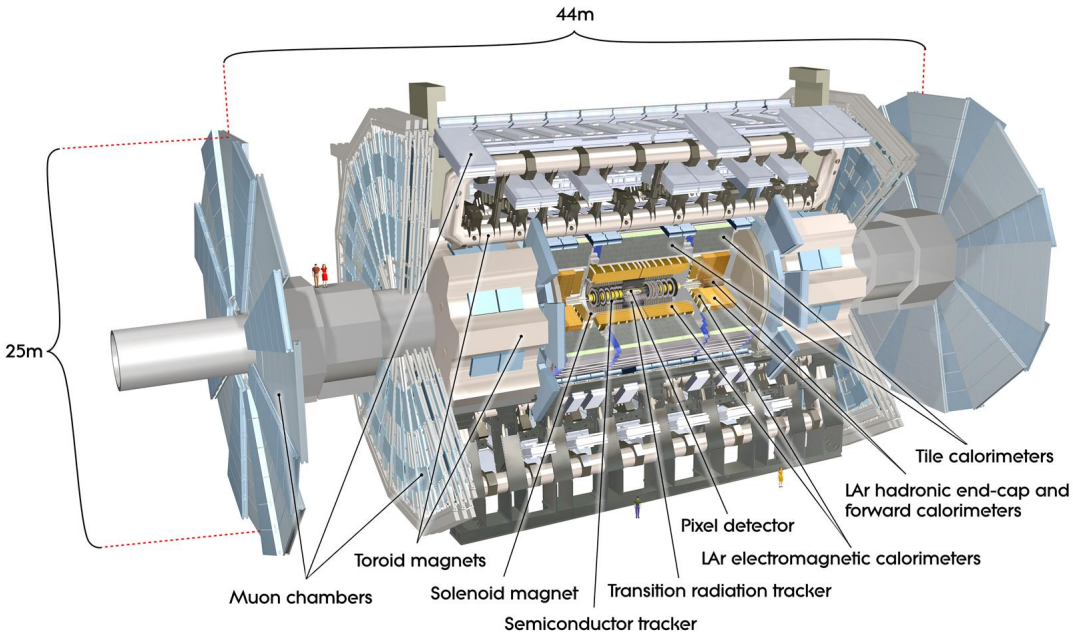

Figure 3.5: The ATLAS detector drawn to scale with its subdetectors [9].

Each subdetector system plays a unique and complementary role in detecting dif-

ferent particles from the proton-proton collisions. The finely segmented inner detector tracks the paths traversed by charged particles. As it is surrounded by the central solenoid, the tracks associated to charged particles bend in different directions (depending on the charge of the particles). The electromagnetic calorimeter is intended to measure the energy deposited by electromagnetically interacting particles, mainly photons and electrons. Then, the hadronic calorimeter detects the energies deposited by hadrons. Unlike the inner tracker, the calorimeters provide energy measurements in a destructive way, i.e. the particles are fully absorbed by material of the calorimeters. Finally, the muon spectrometer detects the tracks of long-lived muons produced during the collisions. It is immersed in strong magnetic fields produced by the barrel and end-cap toroid magnets and this allows the measurement of the energies and momenta on the muons. Figure 3.6 shows a sketch of how particles are detected by the ATLAS detector.

Next, each subdetector system will be described in more detail. More emphasis will be laid on the calorimeters as they play an important role in measuring jets.

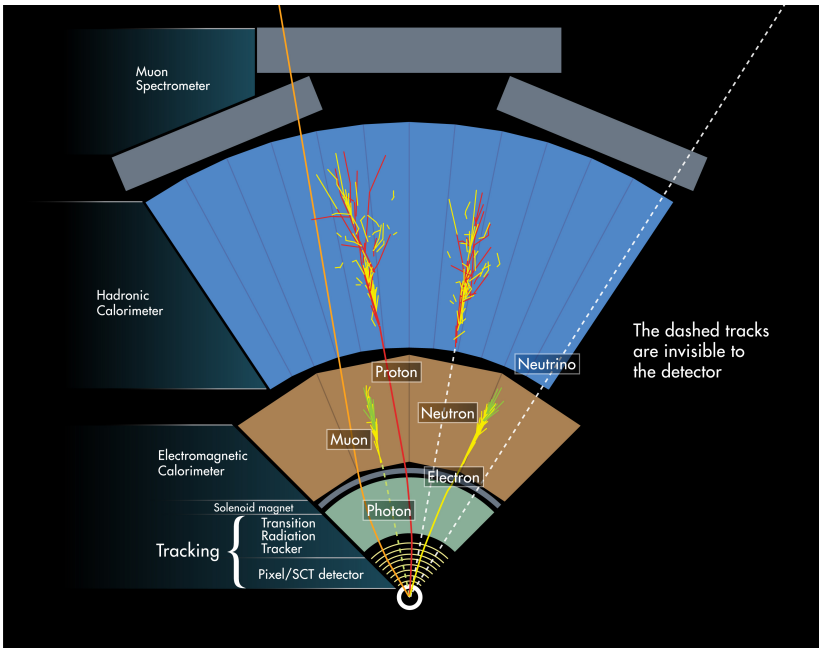

Figure 3.6: The detection of particles by the subdetectors of the ATLAS detector [10].

3.2.1 The Inner Detector

The ATLAS Inner Detector (ID) [60] is designed to provide high-precision measurements of the position and momentum of charged particles produced during the collisions. It is contained in a cylindrical enclosure of length 7 m and radius 1.15 m and is enveloped by the barrel solenoid magnet, which produces a magnetic field of 2 T. The ID detects charged tracks, with p_{T} greater than 0.5 GeV, within the pseudorapidity range $|\eta| < 2.5$ using a combination of three detector technologies: the Pixel detector, the Semi-Conductor Tracker (SCT) and the Transition Radiation Tracker (TRT). These are illustrated in Figure 3.8 and will be discussed next.

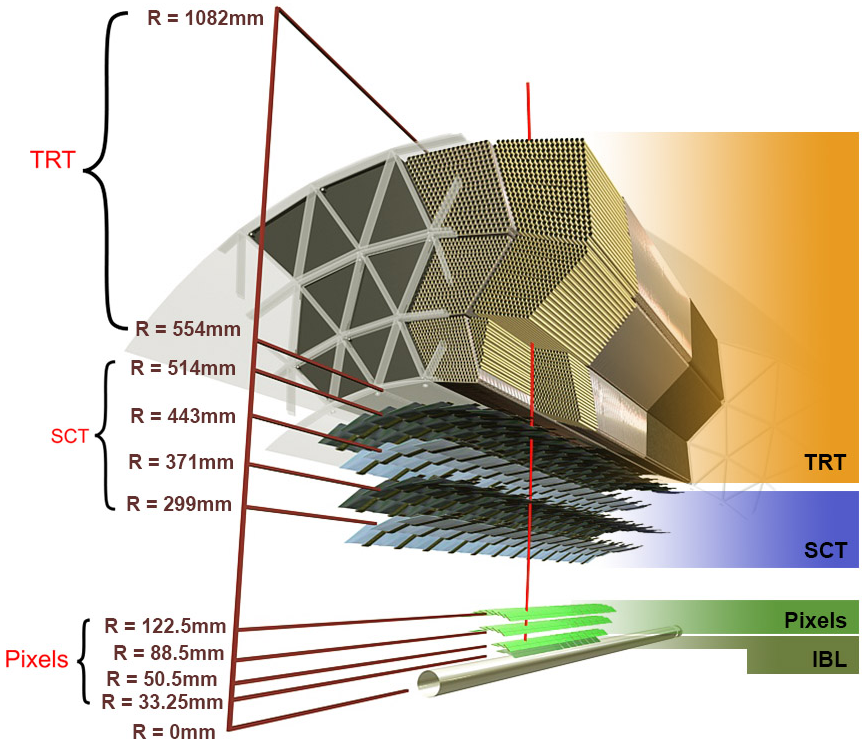

Figure 3.7: A segment of the barrel inner detector of the ATLAS [9].

3.2.1.1 The Pixel Detector

The pixel detector is the innermost detector of the ID. It plays an important role in accurately identifying the multiple collision vertices coming from the proton-proton

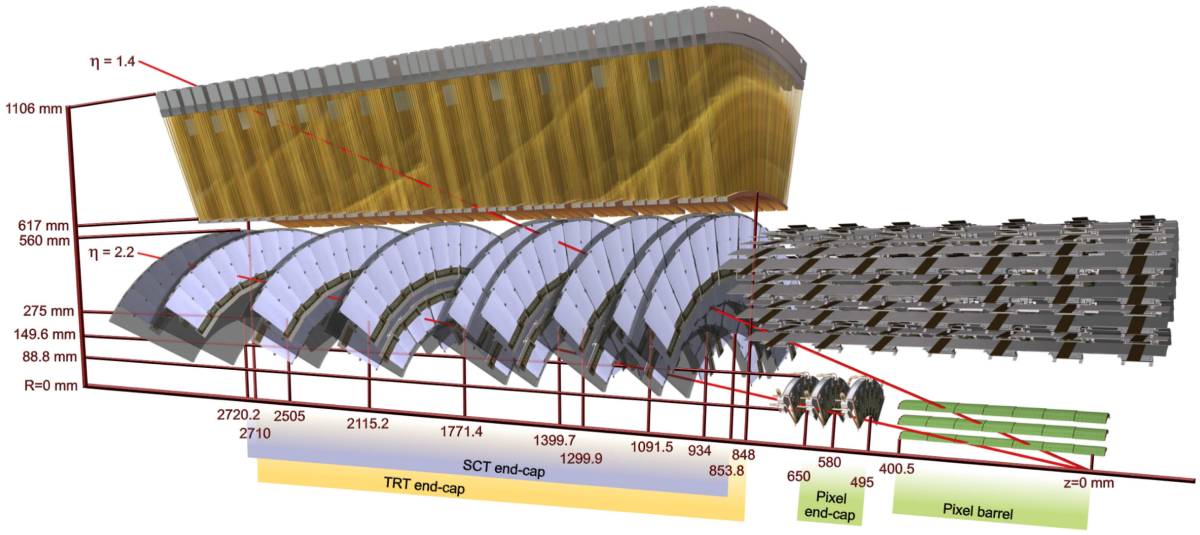

Figure 3.8: A segment of an end-cap inner detector of the ATLAS [9].

interaction region as well as secondary vertices from particles containing a b-quarks. It is arranged in ten layers: four cylindrical barrel layers concentrically surrounding the beam pipe and six disk layers (known as the endcaps), three each at the end of the two sides of the barrel layers. Each layer contains pixel modules which contain a sensor area and various readout electronics. Excluding the innermost barrel layer, there are 1744 pixel modules with dimensions 19 mm $\times$ 63 mm each. To meet the stringent specifications on resolution, occupancy and radiation-hardness, the sensors are made of oxygenated n-type silicon wafers of thickness 250 μm. Each sensor contain 47232 pixels with a nominal pixel size of 50 μm in the R-ϕ plane and 400 μm along the z axis. For identifying points produced by a traveling charged particle, this provides a spacial resolution of (R-ϕ) $\times$ z = 10 μm $\times$ 115 μm. The innermost barrel layer is known as the insertable B-layer (IBL) and was installed in 2014 to cope with high radiation and occupancy. It uses faster read-out electronics, two different silicon sensor technologies, reduced pixel sizes of (R-ϕ) $\times$ z = 50 μm $\times$ 250 μm and new carbon foam structures to support the modules [61]. The reduced pixel size provide a spacial resolution of (R-ϕ) $\times$ z = 8 μm $\times$ 40 μm.

Including the IBL, the ID has approximately 88.4 million electronic readout channels. Figure 3.9 (a), (b) show a pixel module and half of an assembled barrel layer, respectively.

3.2.1.2 The Semi-Conductor Tracker

The SCT surrounds the pixel detector and is the second layer of the ID. It is arranged in twenty-two layers: four cylindrical barrel layers and eighteen disk layers, nine on each endcap. In the barrel region, the SCT is designed to provide at least four precision space-point measurements in the $(\mathrm{R}-\phi), \mathrm{z}$ coordinates using 4 pairs of small-angle stereo strips. The stereo strips are created by laying out two individual strips at an angle of 40 mrad. Each layer is made of p-n silicon semiconductor modules of nominal size 6.36 cm $\times$ 6.40 cm with 780 readout strips. Each strip has length 12 cm and pitch 80 μm. The spatial hit resolution of the strips is (R-ϕ) $\times$ z = 17 μm $\times$ 580 μm. The end-cap modules are very similar in construction but use tapered strips with one set aligned radially.

The SCT has a total of 6.3 million readout channels. Figure 3.9 (c), (d) show a module and the assembled barrel SCT, respectively.

3.2.1.3 The Transition Radiation Tracker

The outermost layer of the ID is the TRT. It is made of 4 mm diameter polyimide tubes filled with a mixture of gases: 70% Argon, 27% CO_2 and 3% O_2. At the center of each tube, there is a 31 μm diameter tungsten wire plated with $0.5-0.7$ μm gold held in place with an end-plug. The barrel region has $50,000$ longitudinally arranged tubes with length 144 cm, and in the end-caps there are $320,000$ radially-arranged tubes with length 32 cm. The tube wall is kept at a high voltage of -1.5 kV and acts as the cathode and the wire is kept at ground and it acts as the anode. As charged particles cross a tube, they ionize the gas, creating electrons that drift to the

anode. This drift-time measurement provides a signal proportional to the energy of the particle and on average, each particle track hits 36 tubes. Each tube provides a spatial hit resolution of 130 μm in a plane perpendicular to the wire.

The total number of TRT readout channels is approximately $351,000$. Figure 3.9 (e), (f) show a TRT tubes and the assembled barrel TRT, respectively.

3.2.2 The Calorimeters

The calorimeter system of ATLAS is located around the ID and functions to measure the energy of particles produced during the collisions. It is finely segmented in the η and ϕ direction and covers the full azimuthal range and $|\eta| < 4.9$. It is made of five subsystems: the Tile Barrel Hadronic Calorimeter (TileCal), the Electromagnetic Barrel Calorimeter (EMB), the Electromagnetic End-Cap Calorimeter (EMEC), the Hadronic End-Cap Calorimeter (HEC) and the LAr Forward Calorimeter (FCal). The Electromagnetic Calorimeters (ECal) measure the energy of particles that interact electromagnetically, e.g. electrons and photons. On the other hand, the Hadronic Calorimeters (HCal) measure the energy of particles that interact via the strong force, e.g. pions and kaons. Particles that interact both electromagnetically and strongly deposit energy in both the ECal and HCal. Figure 3.10 shows a cutaway view of the calorimeter system of ATLAS.

The calorimeters are made of alternating layers of active and passive material. Incoming particles produce a cascade of successively lower-energy particles (known as a particle shower) by interacting with the dense passive material of the calorimeters. The cascade continues until the entire energy of the incoming particle is exhausted. The active layers collect the energy of particles via ionization (ECal) or scintillation (HCal) and the passive layers act as absorbers.

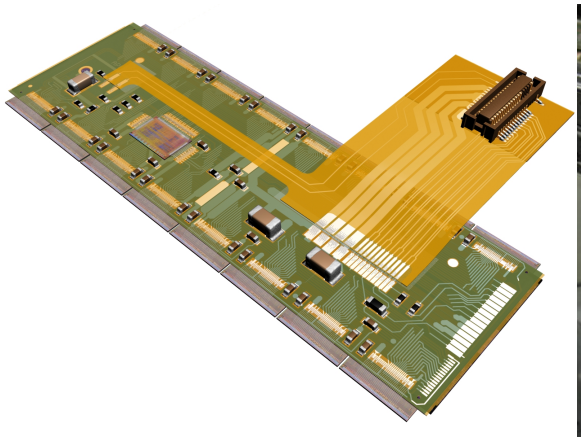

(a) A pixel module

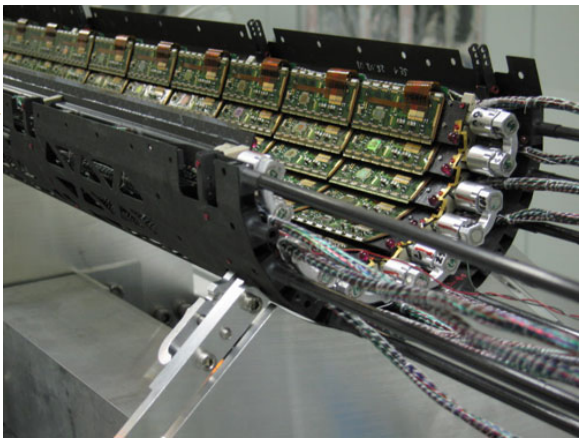

(b) A barrel layer of the pixel detector

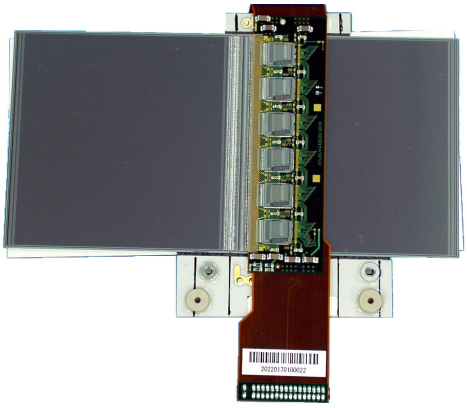

(c) A SCT module

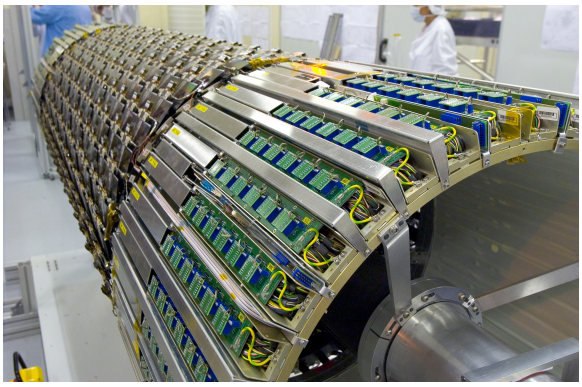

(d) Assembeled barrel SCT

(e) TRT tubes

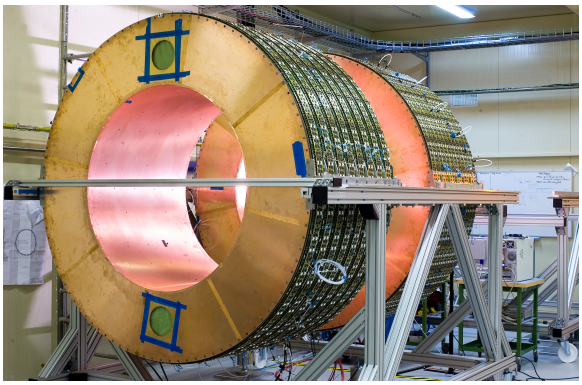

(f) Assembeled barrel TRT

Figure 3.9: The three ID detectors and their modules: (a), (b) the pixel detector [11], [12], (c), (d) the semiconductor tracker [13], [14] and (e), (f) the transition radiation tracker [15], [16].

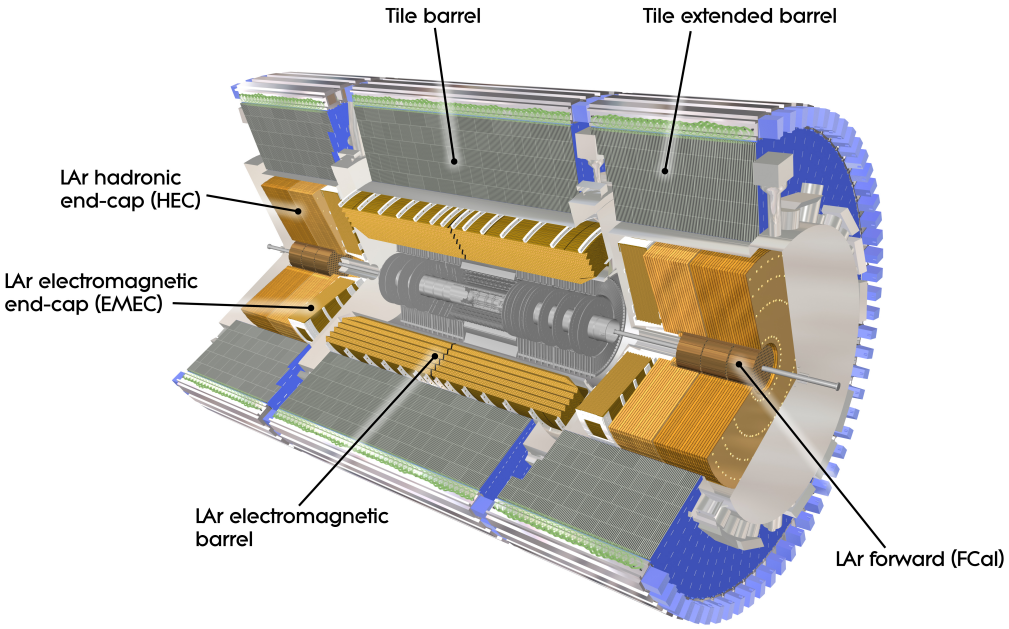

Figure 3.10: Diagram of the ATLAS detector calorimeter system in cutaway view [17].

3.2.2.1 The Electromagnetic Calorimeters

The electromagnetic calorimeters [62] directly surround the ID and barrel solenoid magnet. They are lead and Liquid-Argon (LAr) detectors with accordion-shaped kapton electrodes, where the accordion geometry provides a full, gap-less azimuthal coverage. The liquid argon serves as the active material due to its radiation hardness and the lead absorber plates act as the passive material.

The electromagnetic calorimeters are divided into three parts: the barrel (EMB) ($|\eta| < 1.475$), the end-caps (EMEC) ($1.375 < |\eta| < 3.2$) and the first section of the forward calorimeters, known as FCal1 ($3.1 < |\eta| < 4.9$)[4]. The EMB is made of two half-barrels, separated by 4 mm at z = 0. It is 6.4 m long and has an inner and outer diameter of 2.8 m and 4 m respectively. In total, the EMB is made of 2048 accordion-shaped absorbers, interleaved with readout electrodes. The electrodes are positioned in the middle of two absorbers (2.1 mm from each absorber) by honeycomb

[4]FCal1 has copper absorber plates instead of lead.

spacers. The EMB is segmented in three layers in depth, as shown in Figure 3.11. The first layer is finely segmented in the η direction. The second layer has square cells

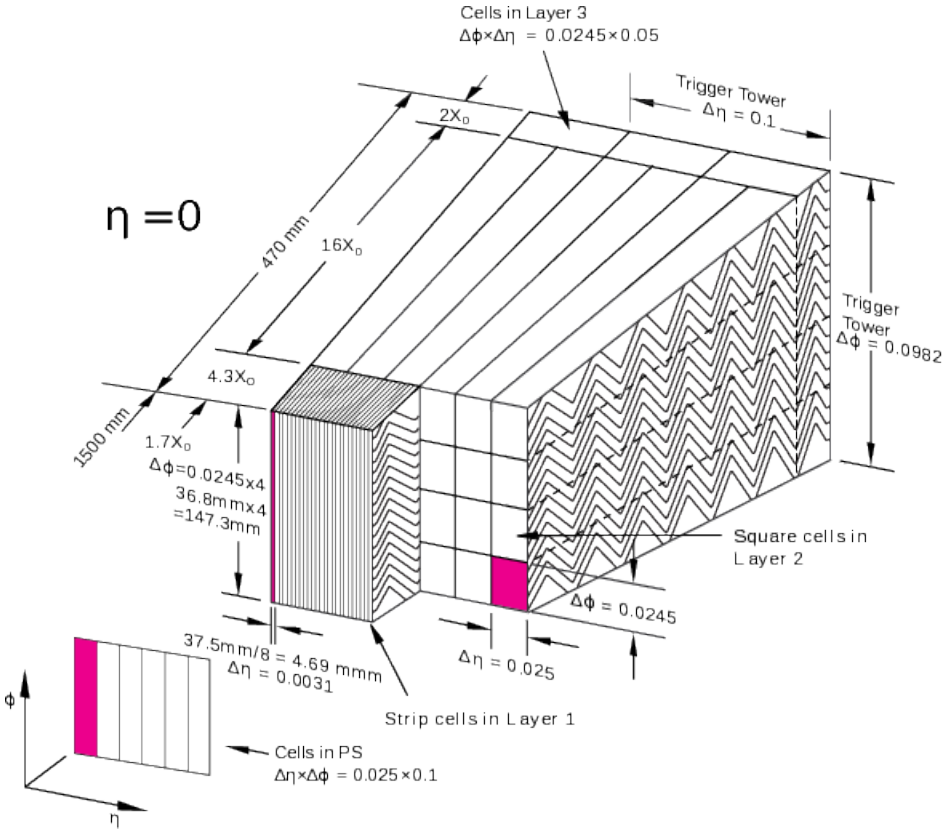

Figure 3.11: The three layers of the barrel electromagnetic calorimeter [9].

of dimension $\Delta\eta \times \Delta\phi = 0.025 \times 0.025$ and the third layer has twice the granularity in η. A separate 11 mm deep LAr layer, known as the presampler (PS), is inserted in front of the first layer and it provides a coverage of $|\eta| < 1.475$. Including the PS, the EMB has $109,568$ readout cells. The PS, three EMB layers and the vast number of cells provide excellent electromagnetic shower sampling. The EMEC consist of two wheels, one on each side of the EMB. It is also segmented into three layers in depth with an additional PS layer covering $1.5 < |\eta| < 1.8$. In total, each end-cap has $31,872$ readout channels.

3.2.2.2 The Hadronic Calorimeters

The hadronic calorimeters [63] surround the ECal. They consist of the barrel TileCal ($|\eta| < 1.7$), the end-cap HEC ($1.5 < |\eta| < 3.2$) and the two remaining FCals: FCal2, FCal3 ($3.1 < |\eta| < 4.9$). The calorimeters use steel as the absorber and polystyrene scintillating tiles as the active material.

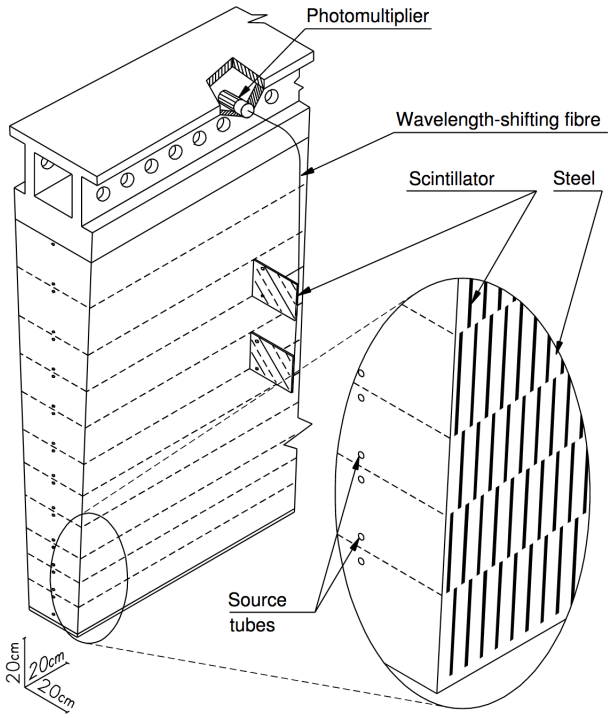

Figure 3.12: The three layers of the barrel electromagnetic calorimeter [9].

The TileCal is divided into two regions: the barrel ($|\eta| < 1.0$) and the extended-barrel ($0.8 < |\eta| < 1.7$) region. Both region are divided azimuthally into 64 modules that are further divided into three layers. The modules extend from an inner radius of 2.28 m to an outer radius of 4.25 m. A single module with alternating steel and scintillating tiles is shown in Figure 3.12. Wavelength-shifting fibers are used to connect the tiles to Photomultiplier Tubes (PMT) at the edge of the modules. This matches the scintillator wavelength to the PMT sensitivity. The PMTs amplify the scintillator signal produced due to passing particles and convert it to an electrical

signal. In total, the HCal uses 9,852 PMTs.

The HEC contains two separate wheels per end-cap. They are located directly behind the EMEC. Each wheel is built using 32 wedge-shaped modules that contain copper plates (passive material) interleaved with LAr (active material). The FCal2 and FCal3 detectors use tungsten at the passive material and LAr as the active material. Each module contains the metal matrix with electrode channels parallel to the beam axis. The HEC and FCals share the cryostat with the EMEC.

(a) Accordion-shpae of EMB layer

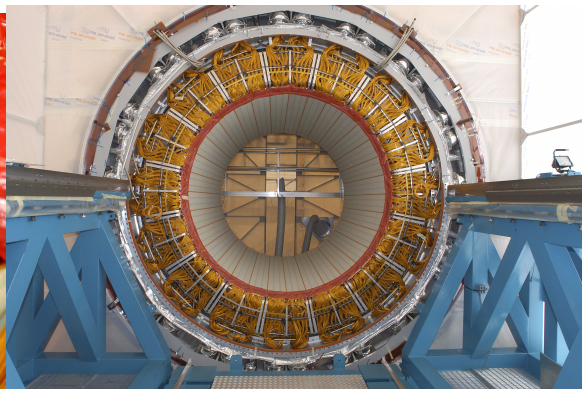

(b) Fully cabled EMB

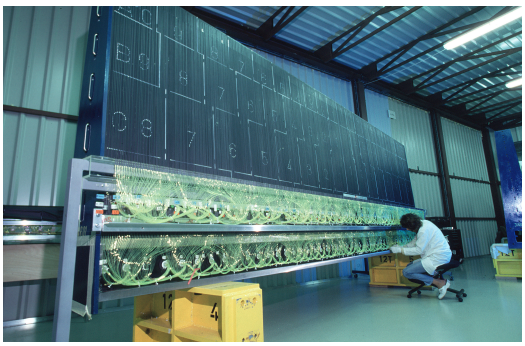

(c) TileCal module

(d) Collection of TileCal modules

Figure 3.13: (a) The accordion-like shape of the electromagnetic barrel calorimeter's absorbers and spacers [18], (b) fully assembled and cabled electromagnetic barrel calorimeter [19], (c) a tile calorimeter module [20], (d) storage of the tile calorimeter modules [21].